IEEE Access
Multidisciplinary | Rapid Review | Open Access Journal

Received September 13, 2019, accepted October 12, 2019, date of publication October 29, 2019,
date of current version November 19, 2019.

Digital Object Identifier 10.1109/ACCESS.2019.2950256

High-Frequency Injection-Based Sensorless Control for a General Five-Phase BLDC Motor Incorporating System Delay and Phase Resistance

BING TIAN[1], QUN-TAO AN[2], (Member, IEEE), AND MARTA MOLINAS[1], (Member, IEEE)
[1]Department of Engineering Cybernetics, Norwegian University of Science and Technology, 7034 Trondheim, Norway
[2]Department of Electrical Engineering, Harbin Institute of Technology, Harbin 150080, China

Corresponding author: Qun-Tao An (anquntao@163.com)

The work was supported in part by the Postdoctoral Fellowship Program of NTNU under Grant 90334705.

ABSTRACT This paper investigates the sensorless control of a general Five-phase permanent magnet brushless DC (5Φ-BLDC) motor working at the low speeds. High frequency (HF) injection-based sensorless control is most popular, however, the system delay and stator resistance could deteriorate the sensorless control performance. In this paper, an HF model of 5Φ BLDCs at frequency-domain is primarily established as a replacement over the conventional static model, and an interpretation from the sinusoidal internal model is carried out to direct the sensorless control implementation. Accordingly, the measured d-axis HF current, which is typically neglected in the conventional method, is reused to demodulate the position angular information from the measured q-axis HF current. The proposed sensorless control is performed on a 5Φ BLDC drive, and experimental results confirm the effectiveness of this method while comparing its performance with the conventional method.

INDEX TERMS Sinusoidal internal model, high-frequency injection, five-phase BLDC motor, sensorless control.

I. INTRODUCTION

Due to its high-power density and high reliability as well as the excellent fault-tolerant capacities, the multi-phase machine has attracted tremendous attention in recent years and has been replacing three-phase (3Φ) motor drive in many applications [1], [2]. In several specified applications, some of these outstanding features may be required to be enhanced early in the motor design stage, and this implies the other features are probably weakened as a compromise. For instance, the fault-tolerant capacities are mostly appreciated in the safety-crucial fields. In this regard, the motor is subject to a modular design and presents low mutual inductances between phases for the sake of magnetic and thermal isolation. Given this, the independent inverter for each phase winding is more suitable for this type of fault-tolerant motor [3]. While in the electric propulsion and electric vehicle systems, the high-power density shall be primarily fulfilled because the motor drive is supposed to work in a very compact environment. In this consideration, the motor tends to have a trapezoidal Back-EMF and extra reluctance torque for improving the torque production. The former type of motor is termed a fault-tolerant motor (FTM) in the previous literature whereas the latter is referred to as a BLDC motor [4]–[6]. In a five-phase (5Φ) BLDC motor, the stator windings are wounded in a trapezoidal manner and give a trapezoidal back EMF. In order to improve the power density, the phase current fed to BLDC motor is also of the quasi-rectangular shape which mainly consists of the fundamental and third harmonics. The 5Φ BLDC with a star-connected stator winding is more general in most applications due to its simplicity in the structure design and manufacturing, but its vector control can be quite burdensome in computation. For instance, the decoupled model of a BLDC motor is represented in two separated rotating sub-spaces [7], and consequently, the Filed Oriented Control (FOC) can be complex which comprises four current PI regulators and a quite involved SVPWM (space voltage PWM) scheme. Apart from the motor structural design, the fault-tolerant performance of 5Ph drives can also be enhanced from the aspect of the software, i.e., the fault-tolerant control (FTC) algorithms [1], [3], [6], [8]. Currently, most available articles concentrate on the disturbance-free

The associate editor coordinating the review of this manuscript and approving it for publication was Atif Iqbal.

operation of the multiphase drive with the failure of one or more phases. By maintaining undisturbed rotating Magneto-Motive Force (MMF) before and after the fault, the multiphase machine still operates properly only by the reconfiguration of remaining phase currents, and thus the reliabilities of multiphase drive can be further improved. Generally, the fault in the mechanical position sensor is also a common type of inadvertent failure. To guarantee the FOC of multiphase drives, sensorless control should be developed as a backup strategy in case of the failure of mechanical position sensors. However, due to the ever-increasing complexity of FOC, only limited computational resources of the adopted digital controller can be allocated for the sensorless control scheme, and this implies the sensorless control, which is fairly simple and effective, is very much appreciated in the case of 5Φ BLDC drives.

The sensorless control of three-phase (3Φ) motor drives has been extensively discussed in the literature, and it falls into two categories: the fundamental model-based method and the saliency tracking-based method [9], [10]. Of these, the former method usually utilizes the back Electromotive Force (EMF) observer or flux linkage observer for the estimation of the rotor position. Among the techniques of reconstructing back-EMFs, the sliding mode observer stands out due to less sensitivity to mismatched uncertainties [9]. However, at low speeds, the back EMFs are too small to observe and thus these methods usually fail. At low speeds, the saliency tracking-based method appears as an alternative solution without recourse to the machine model [10]. This method is realized by continuously superimposing a high frequency (HF) signal upon the fundamental voltage or current, hence even in the absence of fundamental currents, the rotor position can still be recognized by using HF signals. The HF injection based sensorless control has been widely used in 3Φ drives, and tens of thousands of articles have been published since it was first presented. Basically, the 5Φ BLDC includes a sub-model which can be represented by a 3Φ PMSM model, thus the prior review of the techniques that are originally intended for 3Φ PMSMs is meaningful to the successful sensorless control of a 5Φ BLDC.

The state of the art method is the injection of an HF sinusoidal signal from the (estimated) d-axis which helps to mitigate torque oscillation, and this method can be further divided into sinusoidal current and voltage injections. The sinusoidal voltage injection possesses the advantage of the ease of implementation and thereby is dominant in most applications. Recently, the sinusoidal current injection also gains some attention where quasi-resonant controllers (QRC) are adopted to track HF currents [11]. Nevertheless, the zero-error tracking control of HF signals is still difficult due to the sample and zero-hold effect [12], and most importantly, the inclusion of QRC increases the risk of system instability and thus should be carefully designed.

In the sinusoidal signal injection, the convergence time of position or speed estimate is sluggish due to the frequency discrimination filters, e.g., the high-pass filter (HPF) and band-pass filters (BPFs) during HF signal separation [13]. Yoon *et al.* [14], first put forward a square-wave injection for the purpose of extending the bandwidth of position estimation as well as the speed operation range. The injection frequency is up to a half of the switching frequency (in some literature this frequency equals the switching frequency [15]) [16] and a non-filter based HF separation methodology is adopted, instead of the BPF or HPF. Through, an improved dynamic within the full speed range is achieved, this method is susceptible to system noises and measurement errors. In [17], an orthogonal square-wave voltage injection, of which the frequency is one-quarter of the switching frequency, is presented as a replacement over the classical rotating HF injection. However, only a low-speed sensorless control is accomplished, rather than the expected full speed range. Except for the digital delay, this method also raises serious concerns about the dc voltage utilization. That is, the magnitude of square-wave voltage has to be increased remarkably, in order to induce sufficient HF currents that can be sensed by the digital controller, and this can easily lead to the PWM over-modulation. Besides, the modulation of ultra-high frequency voltage via inverter chopping maybe not as efficient as it seems. This problem is aware of in [18], and an asymmetrical SVPWM is suggested to modulate the square-wave voltage. Additionally, thermal issues due to ultra-high frequency injection may cause irreversible demagnetization of PMs, and thereby this ultra-high frequency injection method is typically avoided in the industrial applications. Consequently, the effort of pursuing full speed range sensorless control seems to be fading, and a decent frequency injection around several hundred Hz is in the ascendant. For instance, Yousefi-Talouki *et al.* [19], combined the active flux and classical HF injection for sensorless direct-flux vector control of synchronous reluctance machines, with proven adaptability. Sensorless control of three-phase four-switch inverter-driven motor with merely one single current sensor is investigated under 1 kHz injection [20]. Besides, in [21], the combination of high-bandwidth power switch SIC (working at 100 kHz) with a high-end FPGA is attempted under a 2 kHz injection (which is still classified as a typical HF injection while comparing with the switching frequency).

The typical HF injection (FFI) produces harsh noises that may impact the customer experience in some special applications. In this consideration, a pseudorandom (or variable) frequency injection (PFI), which is claimed to be able to reduce audible noises, emerges as a hot topic regarding the household appliances. In this methodology, the injection frequency usually varies between several alternative frequencies. Since the injection frequency is inconstant, the bandwidth of the incorporated HPFs or BPFs (during the HF signal separation), as well as their natural frequencies, are also supposed to follow the change of the injection frequencies [22]. Regardless of the indispensable frequency adaptive BPF (which is quite time consuming compared to its fixed frequency counterpart), the system delay has also to be considered during the HF signal discrimination. The time delays have limited impacts

on the fundamental current/voltage; however, they can be comparable to the injected HF signal. Du *et al.* [22], proposed a bandwidth tunable resonant controller with a phase lead correction (which is 2 sampling periods prior), to enhance the tracking performance of HF currents whose frequency, however, varies. Zhang *et al.* [23], developed a delay-tolerant scheme to cancel the overall system delay in the implementation of PFI. In addition to this, in [24], a zero-voltage vector injection, which is reported to be capable to reduce audible noises, is presented along with a modified SVPWM. However, the rotor position estimate, which is demodulated from the derivative of the sampled currents, can be quite susceptible to system noises as well as measurement errors. On the other hand, audible noise is also possible to be reduced by lowering the injection frequency. In [25], a low-frequency square-wave voltage (120V/50Hz) injection is presented to estimate the rotor position, but, Nimura *et al.* [13], claims that the filter for signal separation can degrade the current dynamics under a low frequency (LF) injection. To address this, an LF current estimator, which is parameter-dependent, is proposed to remove the LF component of the feedback current. However, the estimator is established on the premise that the estimated d-q frame has been well aligned with the actual one, and this means the presented estimation is probably inaccurate once a deviation occurs between these two frames. Another issue worthy of concern is the phase resistance during the separation of the injection frequency signals. The phase resistance is comparable to the phase reactance under the LF injection and thus cannot be ignored any longer. As noted in [13] that the stator resistance could lead to a considerable estimation error.

To sum up, the fixed high-frequency voltage injection, which has been intensively investigated in the literature, is still appealing in many fields due to its simplicity and robustness. The recently emerged advanced injections, either ultra-high frequency injection, or variable-frequency injection, or low-frequency injection, are, to some extent, adapted from this most basic HF injection scheme. Though certain specific performance can be enhanced with these advanced injections, the defects are also obvious. To the authors' knowledge, a slightly lowered injection frequency is attractive considering today's hardware technologies, and it also benefits from the reduced audible noise, the increased frequency resolution of the injected signal, reduced iron loss, and a preserved DC bus usage. However, as aforementioned the injection frequency cannot be too low otherwise the stator resistance will be dominant which makes it difficult to perform the frequency discrimination. In short, the injection frequency should be carefully designed to improve the sensorless control performance, and this is one purpose of this paper.

In the previous literature, a simplified static HF model is always employed to help perform the sensorless control. However, this is insufficient to solve problems in connection with system delay, stator resistance, and injection frequency optimization. To this end, this work goes one step further by developing a frequency-domain HF model for a general 5Φ BLDC motor in consideration of the above issues. An interpretation of the sensorless control from the sinusoidal internal model is presented. Accordingly, the sensorless control performance can be improved by lowering the injection frequency and using a novel position demodulation method basing on Lock-in Amplifier (LIA). To be specific, both the reference and modulated signals are taken from the measured currents, and thanks to this, the influence of system delay and stator resistance are possible to be mitigated.

The remainder of this paper is organized as follows: sector II highlights the challenge in performing the sensorless control of a 5Φ BLDC drive; sector III develops a comprehensive HF motor model incorporating several factors that are somehow neglected in the previous literature; in sector IV details the novelties of this paper which are, respectively, system delay offsetting and injection frequency optimization; in sector V comparative experiments with the classical method are conducted; and lastly sector VI concludes the contribution of this paper.

II. CHALLENGES OF THE SENSORLESS CONTROL OF 5Φ BLDC MOTOR DRIVES

The mathematical model of a 5Φ PMSM at phase stationary fame is complicated, and for the purpose of vector control the transformation of 5Φ motor model to synchronous frame is preferred and it is given by [7], [26], [27]

$$\begin{aligned}\begin{bmatrix} u_{\mathrm{d}} \\ u_{\mathrm{q}} \\ u_{\mathrm{d3}} \\ u_{\mathrm{q3}} \end{bmatrix} &= R_{\mathrm{s}} \begin{bmatrix} i_{\mathrm{d}} \\ i_{\mathrm{q}} \\ i_{\mathrm{d3}} \\ i_{\mathrm{q3}} \end{bmatrix} + \begin{bmatrix} L_{\mathrm{d}} & 0 & L_{13} & 0 \\ 0 & L_{\mathrm{q}} & 0 & L_{13} \\ L_{13} & 0 & L_{\mathrm{d3}} & 0 \\ 0 & L_{13} & 0 & L_{\mathrm{q3}} \end{bmatrix} \frac{d}{dt} \begin{bmatrix} i_{\mathrm{d}} \\ i_{\mathrm{q}} \\ i_{\mathrm{d3}} \\ i_{\mathrm{q3}} \end{bmatrix} \\ &+ \omega \begin{bmatrix} 0 & -L_{\mathrm{q}} & 0 & -L_{13} \\ L_{\mathrm{d}} & 0 & L_{13} & 0 \\ 0 & -3L_{13} & 0 & -3L_{\mathrm{q3}} \\ 3L_{13} & 0 & 3L_{\mathrm{d3}} & 0 \end{bmatrix} \begin{bmatrix} i_{\mathrm{d}} \\ i_{\mathrm{q}} \\ i_{\mathrm{d3}} \\ i_{\mathrm{q3}} \end{bmatrix} \\ &+ \omega \begin{bmatrix} 0 \\ \psi_{\mathrm{m1}} \\ 0 \\ 3\psi_{\mathrm{m3}} \end{bmatrix} \end{aligned} \tag{1}$$

where u_{d}, u_{q} are the fundamental voltages projected into the synchronous speed rotating space (fundamental subspace); i_{d}, i_{q} fundamental subspace currents; u_{d3}, u_{q3} third harmonic voltages projected into three times synchronous speed rotating space (third subspace); i_{d3}, i_{q3} third subspace currents; L_d, L_q fundamental subspace inductances; L_{d3}, L_{q3} third subspace inductances; L_{13} mutual-inductance between fundamental and third subspaces; λ_{m1}, λ_{m3} fundamental and 3rd harmonic of PM flux linkages; R phase resistance; and ω electrical angular speed.

With extended Clarke and Park transformations, stator currents of fundamental and third subspaces get decoupled from the rotor position and can be controlled separately. For a 5Φ BLDC motor, the stator current is controlled in a quasi-rectangular waveform to match the trapezoidal back EMFs. To achieve this, the third subspace currents (i.e., $i_{d3} = 0$ and $i_{q3} =$ constant) are applied into motor windings whereas the rotor position is obtained with an encoder or a resolver. This is quite different from a 3Φ-BLDC where quasi-rectangular wave current is achieved by a six-step phase commutation. Consequently, the torque profile of 5Φ BLDC motors is much smoother but at the expense of using a mechanical position sensor. To remove the fragile mechanical sensor, sensorless control should be developed.

Figure 1 shows the block diagram of the widely investigated sensorless control in the case of a 5Φ BLDC drive. In this diagram, an ideal HF voltage reference (represented by $V_{inj}\cos\omega_{\rm inj}t$) is injected into the (estimated) d-axis, and then following a position estimator one can derive the position estimate which is, in turn, fed to the FOC. To ensure this HF voltage is of the pure cosine function and not contaminated by the output of the d-axis PI controller, a d-axis LPF (usually a 2nd order LPF) is added into the d-axis current closed-loop. The HF component of $i_{\rm d}$ is considerable and difficult to be fully removed by merely the PI regulator, and thus the usage of $\rm LPF_1$ is unavoidable. Obviously, the presence of $\rm LPF_1$ degrades the current loop dynamics and may even lead to instabilities [13], [28]. In this consideration, it is imperative to cancel $\rm LPF_1$.

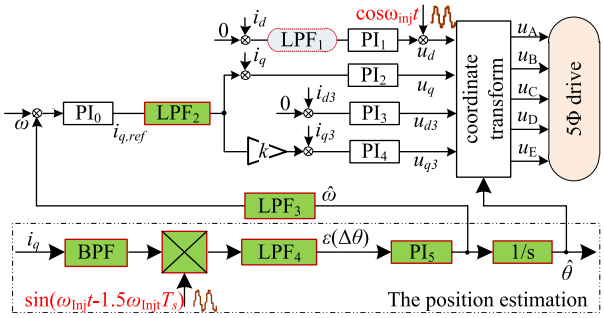

FIGURE 1. Block diagram of the widely investigated sensorless control in the case of a 5Φ BLDC drive.

One additional LPF (i.e., $\rm LPF_2$) is also incorporated to reject the unexpected harmonics in the event of $i_{\rm q,ref}$ step change. In other words, in the transient state, it is difficult to discriminate the expected signal from interferences, however, this problem can be alleviated by including $\rm LPF_2$. The presence of $\rm LPF_2$ degrades the speed loop dynamics, however, this is unavoidable for a robust speed control due to the need for attenuating signals at the unwanted frequencies.

On the other side, in an inverter-driven motor drive, the HF current of interest is distorted due to the PWM updating mode, system noises, zero-order hold effect, etc. The system noises can be suppressed by digital BPFs which, however, introduces more digital delays. Besides, the ideal HF voltage reference is leading ahead of the actual HF voltage by one or a half switching period, depending on PWM update modes, and this could cause another time delay to the HF current of interest [22]–[24]. In sum, the phase relationship between the ideal HF voltage reference and the measured HF current becomes indeterministic, therefore the sensorless control performance can be degraded. Currently, a state-of-the-art method to sort out this problem is a time delay compensation method where the overall system delay is assumed 1.5 sampling periods [17], [29], [30]. However, as explained in numerous literature, the system delay is hard to be quantified accurately [23], [31]. To this end, this paper firstly develops an HF motor model incorporating system delays and phase resistance.

In addition to this, due to the ever-increasing complexity of FOC, only limited computational resources of the adopted digital controller can be allocated for the sensorless control scheme, and thus the sensorless control, which is supposed to be fairly simple and effective, is appreciated in 5Φ BLDC drives. This indicates the sensorless control shall not be performed at the expense of increasing the system complexity.

III. FREQUENCY-DOMAIN HF MODEL

To form quasi-rectangular waveform currents, vector control of $i_d = 0$, $i_{d3} = 0$, $i_q =$ constant, and $i_{q3} =$ constant is preferred. The FOC of 5Φ motor is almost the same with a 3Φ drive except that it is performed in two independent sub-spaces. Consequently, sensorless control of a 5Φ BLDC motor at low speeds can take examples from a 3Φ motor drive. In the conventional method, a static HF model representation under a fixed frequency is employed to direct the sensorless control implementation. However, this HF model, where the R and ω have been omitted, is so idealized that it is difficult to infer the lowest feasible injection frequency. Thus, this paper attempts to develop a frequency-domain HF model, incorporating R and ω, and this is crucial to illustrate the proposed sensorless control method. From the viewpoint of small-signal modeling, HF injection-based sensorless control can be interpreted as the injection of a small HF signal over the motor steady-state operation point and inferring motor operation state from the HF responses.

Assume inputs of a perturbed system are

$$\mathbf{u} = \begin{bmatrix} u_{\rm d} + u_{\rm dh} & u_{\rm q} + u_{\rm qh} \end{bmatrix}^{\rm T} \tag{2}$$

where $u_{\rm d}$, $u_{\rm q}$ are static motor terminal voltages, $u_{\rm dh}$, $u_{\rm qh}$ are motor voltage perturbations, and $\mathbf{u}$ denotes system input vector.

The perturbations in the motor state variables can be given by

$$\mathbf{x} = \begin{bmatrix} i_{\rm d} + i_{\rm dh} & i_{\rm q} + i_{\rm qh} \end{bmatrix}^{\rm T} \tag{3}$$

where $i_{\rm d}$, $i_{\rm q}$ are the static motor phase currents, $i_{\rm dh}$, $i_{\rm qh}$ are motor current perturbations, and $\mathbf{x}$ denotes system state vector.

The motor speed is assumed constant because the shaft inertial constant is much larger than the electromagnetic

constant. Thereby, a small signal representation, which is separated from the steady-state working point, can be given by

$$\begin{bmatrix} u_{\mathrm{dh}} \\ u_{\mathrm{qh}} \end{bmatrix} = \begin{bmatrix} R_{\mathrm{s}} + sL_{\mathrm{d}} & -\omega L_{\mathrm{q}} \\ \omega L_{\mathrm{d}} & R_{\mathrm{s}} + sL_{\mathrm{q}} \end{bmatrix} \begin{bmatrix} i_{\mathrm{dh}} \\ i_{\mathrm{qh}} \end{bmatrix} + L_{13} \begin{bmatrix} si_{\mathrm{d3h}} - \omega i_{\mathrm{q3h}} \\ si_{\mathrm{q3h}} + \omega i_{\mathrm{q3h}} \end{bmatrix} \quad (4)$$

It makes no sense to establish a small signal model under the real d-q frame as the rotor position is missing and thus transforming u_{dh} and u_{qh} into the estimated d-q frame yields

$$\begin{bmatrix} u_{\hat{d}h} \\ u_{\hat{q}h} \end{bmatrix} = \begin{bmatrix} \cos\Delta\theta & \sin\Delta\theta \\ -\sin\Delta\theta & \cos\Delta\theta \end{bmatrix} \begin{bmatrix} R_{\mathrm{s}} + sL_{\mathrm{d1}} & -\omega L_{\mathrm{q1}} \\ \omega L_{\mathrm{d1}} & R_{\mathrm{s}} + sL_{\mathrm{q1}} \end{bmatrix} \times \begin{bmatrix} i_{\mathrm{dh}} \\ i_{\mathrm{qh}} \end{bmatrix} + L_{13} \begin{bmatrix} \cos\Delta\theta & \sin\Delta\theta \\ -\sin\Delta\theta & \cos\Delta\theta \end{bmatrix} \times \begin{bmatrix} si_{\mathrm{d3h}} - \omega i_{\mathrm{q3h}} \\ si_{\mathrm{q3h}} + \omega i_{\mathrm{q3h}} \end{bmatrix} \quad (5)$$

where $\Delta\theta$ is the position estimation error, which is given by

$$\Delta\theta = \hat{\theta} - \theta \quad (6)$$

The relationship between real and the estimated d-q frame can be formulated by

$$\begin{bmatrix} i_{\hat{d}h} \\ i_{\hat{q}h} \end{bmatrix} = \begin{bmatrix} \cos\Delta\theta & \sin\Delta\theta \\ -\sin\Delta\theta & \cos\Delta\theta \end{bmatrix} \begin{bmatrix} i_{dh} \\ i_{qh} \end{bmatrix}, \quad \begin{bmatrix} u_{\hat{d}h} \\ u_{\hat{q}h} \end{bmatrix} = \begin{bmatrix} \cos\Delta\theta & \sin\Delta\theta \\ -\sin\Delta\theta & \cos\Delta\theta \end{bmatrix} \begin{bmatrix} u_{dh} \\ u_{qh} \end{bmatrix} \quad (7)$$

$$\begin{bmatrix} i_{\hat{d}3h} \\ i_{\hat{q}3h} \end{bmatrix} = \begin{bmatrix} \cos\Delta\theta & \sin\Delta\theta \\ -\sin\Delta\theta & \cos\Delta\theta \end{bmatrix} \begin{bmatrix} i_{d3h} \\ i_{q3h} \end{bmatrix} \quad (8)$$

In the above equations, symbols with a hat "^" indicate the estimated quantities. From (4), certain current disturbances from 3rd sub-space are coupled into the 1st sub-space via L_{13}, and to simplify the analysis we define

$$\begin{bmatrix} u_{\hat{d}13h} \\ u_{\hat{q}13h} \end{bmatrix} = sL_{13} \begin{bmatrix} i_{\hat{d}3h} \\ i_{\hat{q}3h} \end{bmatrix} \quad (9)$$

where $u_{\hat{d}13h}$, $u_{\hat{q}13h}$ denote voltage disturbances due to the mutual inductance between the 1st sub-space and 3rd sub-space.

Substituting (7) and (8) into (4), it yields a small signal model at an estimated d-q frame

$$\begin{bmatrix} i_{\hat{d}h} \\ i_{\hat{q}h} \end{bmatrix} = \frac{1}{A_0} \begin{bmatrix} A_{11} & A_{12} \\ A_{21} & A_{22} \end{bmatrix} \begin{bmatrix} u_{\hat{d}h} \\ u_{\hat{q}h} \end{bmatrix} - \frac{1}{A_0} \begin{bmatrix} a_{11} & a_{12} \\ a_{21} & a_{22} \end{bmatrix} \begin{bmatrix} u_{\hat{d}13h} \\ u_{\hat{q}13h} \end{bmatrix} \quad (10)$$

where

$$A_0 = L_d L_q s^2 + R_s \left(L_d + L_q\right) s + R_s^2 + L_d L_q \omega^2 \quad (11)$$

and

$$\begin{cases} a_{11} = sL_q + R_s + {\omega^2 L_q}/{s} \\ a_{12} = -{\omega R_s}/{s}, \ a_{21} = {\omega R_s}/{s} \\ a_{22} = sL_d + R_s + {\omega^2 L_d}/{s} \end{cases} \quad (12)$$

$$\begin{cases} A_{11} = -0.5\omega(L_d - L_q)\sin(2\Delta\theta) + R_s \\ \quad +0.5\left[L_d + L_q - (L_d - L_q)\cos(2\Delta\theta)\right]s \\ A_{12} = 0.5\omega\left[L_d + L_q - (L_d - L_q)\cos(2\Delta\theta)\right] \\ \quad +0.5(L_d - L_q)\sin(2\Delta\theta)s \\ A_{21} = -0.5\omega\left[L_d + L_q + (L_d - L_q)\cos(2\Delta\theta)\right] \\ \quad +0.5(L_d - L_q)\sin(2\Delta\theta)s \\ A_{22} = 0.5\omega(L_d - L_q)\sin(2\Delta\theta) + R_s \\ \quad +0.5\left[L_d + L_q - (L_d + L_q)\cos(2\Delta\theta)\right]s \end{cases} \quad (13)$$

where the letter "A" indicates HF admittance.

Figure 2 describes the block diagram of the HF model incorporating the system delay and the phase resistance. In this figure, $I_{\hat{d}h}$, $I_{\hat{q}h}$ are the filtered HF signals, and $U_{\hat{d}h}$, $U_{\hat{q}h}$ are ideal HF voltage references. Obviously, the filtered HF current has a poor correlation with the ideal HF voltage reference because of numerous delays as well as the resistance. To tackle this, the time delay compensation, which is deemed quantifiable, is suggested in some literature, however, this is still not accurate enough.

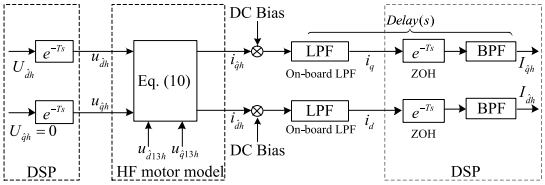

FIGURE 2. The HF motor model incorporating the system delay and the phase resistance.

IV. THE PROPOSED REMEDY METHOD

A. FREQUENCY DOMAIN ANALYSIS

Assume a d-axis voltage injection is applied, which is represented by $\left[U_{\hat{d}h}, U_{\hat{q}h}\right] = \left[U_{\hat{d}h}, 0\right]$, and this results in a delayed HF voltage over the motor winding after inverter chopping. This actual HF voltage excites substantial HF currents that contain the $\Delta\theta$-related information. To remove system noises, including the static current bias, on-board LPFs, and digital 2nd bandpass filters are successively applied. From Figure 2, $I_{\hat{d}h}$ and $i_{\hat{d}h}$ (as well as $I_{\hat{q}h}$ and $i_{\hat{q}h}$) has the following relationship

$$I_{\hat{d}h} = Delay\,(s)\, i_{\hat{d}h}, \quad I_{\hat{q}h} = Delay\,(s)\, i_{\hat{q}h} \quad (14)$$

where $Delay(s)$ indicates the overall system delay during separating HF currents. One the other hand, one can have $\left[u_{\hat{d}13h}, u_{\hat{q}13h}\right] = [0, 0]$ due to the absence of HF currents at 3rd sub-space.

Therefore, Figure 2 can be simplified as the following:

$$\begin{cases} \dfrac{I_{\hat{q}h}}{U_{\hat{d}h}e^{-Ts}Delay\,(s)} = \dfrac{i_{\hat{q}h}}{u_{\hat{d}h}} = K_{iq,\sin}\dfrac{\xi\omega_r^2}{s^2 + \xi\omega_r s + \omega_r^2} \\ \quad +K_{iq,\cos}\dfrac{\xi\omega_r s}{s^2 + \xi\omega_r s + \omega_r^2} \\ \dfrac{I_{\hat{d}h}}{U_{\hat{d}h}e^{-Ts}Delay\,(s)} = \dfrac{i_{\hat{d}h}}{u_{\hat{d}h}} = K_{id,\sin}\dfrac{\xi\omega_r^2}{s^2 + \xi\omega_r s + \omega_r^2} \\ \quad +K_{id,\cos}\dfrac{\xi\omega_r s}{s^2 + \xi\omega_r s + \omega_r^2} \end{cases} \quad (15)$$

where

$$\xi = \frac{R_s}{\omega_r}\left(\frac{1}{L_d}+\frac{1}{L_q}\right), \quad \omega_r = \sqrt{R_s^2 \Big/ L_d L_q + \omega^2} \tag{16}$$

and

$$\begin{cases} K_{iq,\sin} = \dfrac{-0.5\omega\left[L_d + L_q + (L_d - L_q)\cos(2\Delta\theta)\right]}{\omega_r\left(L_d + L_q\right)R_s} \\ K_{iq,\cos} = \dfrac{0.5(L_d - L_q)\sin(2\Delta\theta)}{\left(L_d + L_q\right)R_s} \\ K_{id,\sin} = \dfrac{-0.5\omega(L_d - L_q)\sin(2\Delta\theta) + R_s}{\omega_r L_d L_q \xi} \\ K_{id,\cos} = \dfrac{0.5\left[L_d + L_q - (L_d - L_q)\cos(2\Delta\theta)\right]}{L_d L_q \xi} \end{cases} \tag{17}$$

In the above equations, ω_r is the natural frequency of this plant model; ξ is the damping factor; and $k_{iq,\sin}$, $k_{iq,\cos}$, $k_{id,\sin}$, $k_{id,\cos}$ are gains that possess special meanings related to sinusoidal internal models.

Now consider the Laplace transform of sine (or cosine) functions, which is the model transformation to the frequency domain from the time-domain [32], [33].

$$\begin{aligned} G_{\sin}(s) &= \mathscr{L}\left(\sin\left(\omega_r t\right)\right) = \frac{\omega_r}{s^2+\omega_r^2}, \\ G_{\cos}(s) &= \mathscr{L}\left(\cos\left(\omega_r t\right)\right) = \frac{s}{s^2+\omega_r^2} \end{aligned} \tag{18}$$

where $\mathscr{L}$ denotes the Laplace operator. Actually, (18) always acts as the resonant controller to track the AC reference, and this is one typical application scenario of the internal model principle. However, controllers indicated by (18) are with a narrow bandwidth, and by including a damping factor into the denominators, the bandwidth of transfer-functions in (18) has potential to be expanded, and this yields the following representations

$$\begin{aligned} G_{\text{Quasi-sin}}(s) &= \frac{\xi\omega_r^2}{s^2+\xi\omega_r s+\omega_r^2}, \\ G_{\text{Quasi-cos}}(s) &= \frac{\xi\omega_r s}{s^2+\xi\omega_r s+\omega_r^2} \end{aligned} \tag{19}$$

where $G_{\text{Quasi-sin}}(s)$, and $G_{\text{Quasi-cos}}(s)$ denote, respectively, the quasi-sin and quasi-cos internal model representations.

Clearly, the presented plant model can be viewed as a combination of a quasi-sin and quasi-cos transfer functions, which can be given by

$$\frac{I_{\hat{q}h}}{V_{\hat{d}h}} = K_{iq,\sin}G_{\text{Quasi-sin}}(s) + K_{iq,\cos}G_{\text{Quasi-cos}}(s) \tag{20}$$

$$\frac{I_{\hat{d}h}}{V_{\hat{d}h}} = K_{id,\sin}G_{\text{Quasi-sin}}(s) + K_{id,\cos}G_{\text{Quasi-cos}}(s) \tag{21}$$

$$V_{\hat{d}h} = U_{\hat{d}h}e^{-Ts}Delay\,(s) \tag{22}$$

where $V_{\hat{d}h}$ represents a virtual HF voltage which takes into account the system delay.

Figure 3 shows the bode plots of quasi-sin and quasi-cos sub-plant models. As is evident that a substantial phase lag is generated with regard to the frequency of interest when the injection frequency is improperly lowered. This also explains why the resistance, which is usually ignored, must be carefully re-considered in the case of a lower frequency injection. Besides, in the conventional method, the term $e^{-Ts}Delay\,(s)$ in (22) is modeled to be 1.5 sampling periods, however, this may be not accurate enough in consideration of the hardware delays. Given these, it is urgent to develop a more robust HF-based sensorless control that is immune to system delay and the resistance effect.

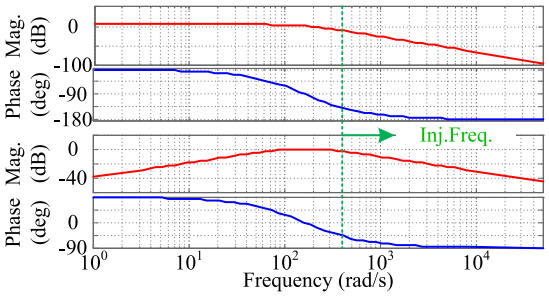

FIGURE 3. Bode plots of the quasi-sin (upper plots) and quasi-cos (lower plots) sub-plant models.

The above dynamic system model plays an important role in the implementation of the proposed sensorless control, and some important properties of the HF plant model have the potential to be disclosed: **1)**: The derived plant model can be viewed as a combination of a quasi-cos sub-plant and a quasi-sin sub-plant. In each frequency, the outputs of these two sub-plants are mutually orthogonal, and this can be easily understood by the orthogonality of sine and cosine functions. **2):** Only quasi-cos sub-plant of (20) is preferred for sensorless control due to that the coefficient $k_{\text{id,cos}}$ contains the $\Delta\theta$-related information whereas the quasi-sin sub-plant acts as a disturbance. The magnitudes of $k_{\text{iq,cos}}$ and $k_{\text{iq,cos}}$ are almost identical, and this indicates the plant output is a fusion of the target signal and disturbance, however, neither of them can be dominant or rather both of them are dominant.

B. PHASE LOCKING OF THE MEASURED d-AXIS HF CURRENT

HF voltage injection is investigated in this paper, and specially, a lock-in amplifier is employed to extract $\Delta\theta$ under the noisy environment. The phase relation between the target and disturbance signals is what we are utmost concerned. According to the principle of correlation detection, the disturbance can be efficiently eliminated by multiplying it with its orthonormal reference and taking the mean value, and this can be understood by the following manipulation [34], [35].

$$\lim_{T\to\infty}\frac{1}{T}\int_0^T A_n\cos(\omega t)\times\sin(\omega t)\mathrm{d}t = 0 \tag{23}$$

where $A_n\cos\omega t$ denotes the disturbance and $\sin\omega t$ is its orthonormal reference.

And the target signal can be reserved in term of a DC signal, which is given by

$$\lim_{T\to\infty}\frac{1}{T}\int_0^T A_T\sin(\omega t)\times\sin(\omega t)\mathrm{d}t=\frac{A_T}{2} \tag{24}$$

where $A_T\sin\omega t$ denotes the target signal.

As aforementioned, the presented plant model can be viewed as a combination of two orthogonal sub-plants where the quasi-sin sub-plant output is a disturbance. However, time-delay compensation represented by $\sin(\omega_{\mathrm{Inj}}t\text{-}1.5\omega_{\mathrm{Inj}}T_s)$ is not enough to suppress disturbances or noises. Therefore, the key to solving this problem changes to finding a standard reference, which is orthogonal to the disturbance, as a replacement over the most-adopted sine function. When reviewing the d-axis HF plant as shown in (21), it is interesting to find that the d-axis HF plant almost possesses similar constituents with the q-axis HF plant. If the d-axis HF plant can be infinitely approximate to a single quasi-cos model, then the problem suffered in the conventional method can be easily resolved.

$$\frac{I_{\hat{d}h}}{V_{\hat{d}h}}\approx K_{id,\cos}G_{\mathrm{Quasi\text{-}cos}}(s) \tag{25}$$

Assume above approximation holds which, however, may be conditional. Equation (25) shares the same internal model with the target sub-plant of (20), and this implies that the target signal, which contains $\Delta\theta$-related information, is always in phase with $I_{\hat{d}h}$ when the estimated d-axis leads ahead of the real d-axis and anti-phased when the estimated d-axis lags behind. Thus, a standard reference in phase with $I_{\hat{d}h}$ is more suitable to extract $\Delta\theta$ in practice. From Figure 2, the d-axis current is delayed concurrently with the q-axis current, and this means no phase shift between them. Then this crucial standard reference can be derived by the following manipulation

$$HF_{ref}=sign\left(I_{\hat{d}h}\right) \tag{26}$$

Actually (26) acts as a phase-lock loop (PLL), and the output of this PLL is also a square waveform. Evidently, this method for locking the phase of the input signal is quite easy to implement and the resulted reference can keep in pace with the input signal dynamically.

C. INJECTION FREQUENCY CHOICE

As aforementioned, (25) may conditionally hold, and this is up to the injection frequency preference. Notice that it is impossible to achieve (25) over all frequencies; however, this approximation at the injection frequency can be at least achieved by applying the following constraint

$$\left|K_{id,\cos}\frac{\xi s}{s^2+\xi s+\omega_r^2}\right|_{s=j\omega_{inj}}\gg\left|K_{id,\sin}\frac{\xi\omega_r}{s^2+\xi s+\omega_r^2}\right|_{s=j\omega_{inj}} \tag{27}$$

where ω_{inj} is the angular frequency of the injected signal. Accordingly, the constraint for the frequency preference can be given by the following constraints

$$\begin{aligned}\omega_{inj}&\geq 10\left|\frac{K_{id,\sin}\omega_r}{K_{id,\cos}}\right|\\&=10\left|\frac{-0.5\omega(L_d-L_q)\sin(2\Delta\theta)+R_s}{0.5\left[L_d+L_q-(L_d-L_q)\cos(2\Delta\theta)\right]}\right|\end{aligned} \tag{28}$$

$$\omega_{inj}=\frac{\omega_{sw}}{n},\quad n=1,2,3,4,5\cdots\cdots \tag{29}$$

$$\omega_{inj}\geq 10\omega \tag{30}$$

where ω_{sw} denotes the switching frequency and is given in the form of the angular frequency. Equation (29) implies that the injection frequency shall be the integer division of switching frequency. For the ease of HF separation, the injection frequency is supposed to be far away from the fundamental frequency.

Assuming the maximum motor speed is about 100 rpm and considering a $\pm10\%$ measurement error (ME) of L_d and L_q as well as a $\pm10^\circ$ position estimation error in the steady state, the feasible minimal injection frequency can be primarily determined, which is plotted in Figure 4. Accordingly, the injection frequency can be lowered to 257.5Hz under the 10.3kHz switching frequency. It has to be noted that this minimum injection frequency can be further lowered in some motor drives with a larger structural saliency.

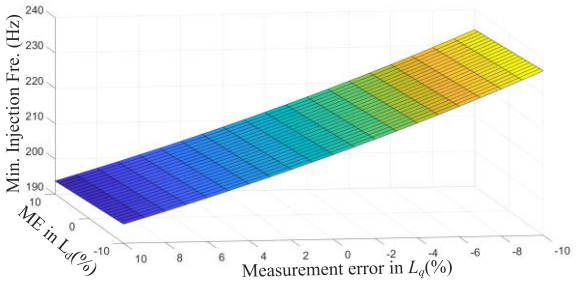

FIGURE 4. Minimum injection frequency of the studied motor.

D. $\Delta\theta$ DEMODULATION

The injected HF voltage can be either a sinusoidal or square-wave signal. However, the square-wave signal is much easier to generate in a Digital Signal Processor (DSP) than the sinusoidal signal, and thus square-wave signal injection is preferred. It must be also noticed that this square-wave injection is different from the traditional one in the previous literature whose frequency is up to 1/2 or 4 of switching frequency [11], [12].

Assume a d-axis square-wave HF voltage is applied into the motor, which can be represented by

$$v_{inj}sign\left(\cos\left(\omega_{inj}t\right)\right)=\frac{4v_{inj}}{\pi}\sum_{n=0}^{\infty}\frac{1}{2n+1}\sin\left((2n+1)\,\omega_{inj}t\right) \tag{31}$$

This signal consists of abundant harmonics where the 1st harmonic (the desired harmonic) is dominant. The higher-order harmonics are almost attenuated by phase inductances and only the 1st harmonic is preserved in the form of the HF current. Notice that this induced HF current can, in turn, contaminate the ideal HF voltage injection through the PI regulator. In conventional methods, a d-axis LPF is employed to filter out these HF currents, which, however, impacts the system stability. In this paper, this LPF can be canceled and therefore the injected HF voltage is a mix of the ideal square wave voltage and the PI output

$$U_{\hat{d}h} = v_{inj} sign\left(\cos\left(\omega_{inj} t\right)\right) + PI(i_{d,ref} - i_d) \tag{32}$$

In this consideration, the virtual HF voltage, which incorporates numerous time delays, can be given by

$$V_{\hat{d}h} = e^{-T_1 s} Delay\,(s)\, U_{\hat{d}h} \approx v_{inj} \cos(\omega_{inj} t - \psi_x) \tag{33}$$

where ψ_x implies that the phase angle of $V_{\hat{d}h}$, which is yet unknown to us.

According to (20) and (21), the induced HF currents can be given by

$$\begin{aligned} I_{\hat{q}h} &= K_{iq,\sin} k_{\sin} v_x \cos\left(\omega_{inj} t - \psi_x - \psi_y\right) \\ &\quad + K_{iq,\cos} k_{\cos} v_x \cos\left(\omega_{inj} t - \psi_x - \psi_y - {}^{\pi}/_{2}\right) \end{aligned} \tag{34}$$

$$\begin{aligned} I_{\hat{d}h} &= V_{\hat{d}h} K_{id,\cos} G_{\text{Quasi-cos}}(s) \\ &= K_{id,\cos} k_{\cos} v_x \cos\left(\omega_{inj} t - \psi_x - \psi_y - {}^{\pi}/_{2}\right) \end{aligned} \tag{35}$$

where ψ_y indicates the phase lag of the quasi-cos transfer function; $k_{\cos}$, and $k_{\sin}$ represent gains of, respectively, quasi-cos and quasi-sin sub-plants at the injection frequency; and the phase lag $\pi/2$ in (34) can be inferred by the orthogonality of quasi-sin and quasi-cos sub-plants. Notice that $\Delta\theta$-related information is contained in the $k_{\text{iq,cos}}$, which can be computed with the aid of $I_{\hat{d}h}$.

Accordingly, the standard reference, which is taken from the measured d-axis current, is given as below

$$\begin{aligned} HF_{ref} &= sign\left(I_{\hat{d}h}\right) = sign\left(\cos\left(\omega_{inj} t - \psi_x - \psi_y - {}^{\pi}/_{2}\right)\right) \\ &= \frac{4}{\pi} \sum_{n=0}^{\infty} \frac{1}{2n+1} \sin\left((2n+1)\left(\omega_{inj} t - \psi_x - \psi_y\right)\right) \end{aligned} \tag{36}$$

In this paper, this square-wave reference, instead of $\sin(\omega_{\text{Inj}} t\text{-}1.5\omega_{\text{Inj}} T_s)$ in Figure 1, is finally used to demodulate position error information from the measured q-axis HF current.

Figure 5 shows the proposed method for position error demodulation which is based on the LIA method. In this figure, Δi_d and Δi_q represent the input errors of PI_1 and PI_2, respectively, of which the DC offset has been removed. The utilized BPF takes the form of the quasi-cos transfer function as shown in (19). The d- and q-axis BPFs work in parallel and share the same preferences, and thus one only needs to focus on one of the BPFs in the filter design. Theoretically, the bandwidth of this BPF can be set to twice the injection frequency, which is supposed to damp the (transient state)

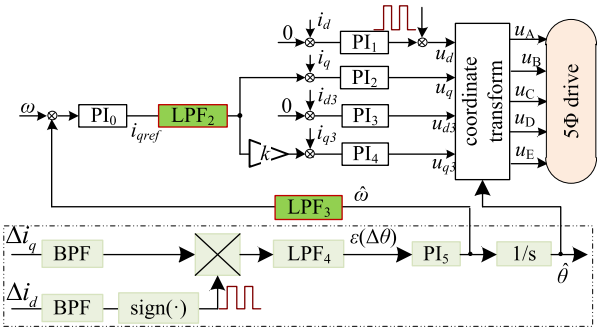

FIGURE 5. Schematic for the proposed sensorless control.

DC offset of Δi_d and Δi_q. However, due to the relatively low sampling rate when measuring the injection frequency, the performance of BPF downgrades a lot. Therefore, in a real drive, the bandwidth is determined through empirical analysis (i.e., trial and error) which is $0.45\omega_r$ in this case.

The product shown in Figure 5 acts as a phase-sensitive detector and multiplying (34) by (36) yields

$$\begin{aligned} Product &= I_{\hat{q}h} \cdot HF_{ref} \\ &= \frac{2K_{iq,\cos} k_{\cos} v_x}{\pi} + \frac{2K_{iq,\cos} k_{\cos} v_x}{\pi} \\ &\quad \times \sum_{n=1}^{\infty} \frac{1}{2n+1} \cos\left(2n\left(\omega_{inj} t - \psi_x - \psi_y\right)\right) \\ &\quad - \frac{2K_{iq,\sin} k_{\sin} v_x}{\pi} \sum_{n=1}^{\infty} \frac{1}{2n+1} \\ &\quad \times \sin\left(2n\left(\omega_{inj} t - \psi_x - \psi_y\right)\right) \\ &\quad - \frac{2K_{iq,\cos} k_{\cos} v_x}{\pi} \sum_{n=0}^{\infty} \frac{1}{2n+1} \\ &\quad \times \cos\left(2\left(n+1\right)\left(\omega_{inj} t - \psi_x - \psi_y\right)\right) \\ &\quad - \frac{2K_{iq,\sin} k_{\sin} v_x}{\pi} \sum_{n=0}^{\infty} \frac{1}{2n+1} \\ &\quad \times \sin\left(2\left(n+1\right)\left(\omega_{inj} t - \psi_x - \psi_y\right)\right) \end{aligned} \tag{37}$$

In the above equation, only the target signal can be transformed into a DC component, whereas the spectrum of disturbances is mapped to twice the frequencies or higher. Thus, the position error information can be identified by passing the product through a 2nd LPF and keeping the mean value, and it can be given by

$$\begin{aligned} \varepsilon\left(\Delta\theta\right) &= LPF_{2nd}(Product) = \frac{2K_{iq,\cos} k_{\cos} v_x}{\pi} \\ &= \frac{2(L_d - L_q) k_{\cos} v_x \Delta\theta}{L_d L_q \xi \pi} \end{aligned} \tag{38}$$

The employed 2nd LPF takes the form of the quasi-sin transfer function as shown in (19). Fortunately, the sampling rate of the LPF is much higher than the frequency to be measured, and this means the filter design can be easier and more idealized. In this paper the measured frequency is 0Hz, and

the unwanted frequencies are twice the injection frequency. In this consideration, the cutoff frequency of the 2nd LPF is set to 51.5Hz, and the attenuation rate beyond the cutoff frequency is 40 dB/dec. As $\Delta\theta$ can be precisely measured in the proposed method, this indicates that position estimation accuracy has the potential to be improved. The rotor speed and position estimates can be obtained by the PI and the followed integrator in Figure 5, and the cut-off frequency setting of LPF_3 is referenced to the rotational inertial of the studied motor drive. Consequently, the speed dynamic of sensorless control is relatively slow compared to the version with a mechanical position sensor. This can be explained by the fact that it always necessitates several injection cycles to estimate a reliable position with the sensorless control scheme, whereas this crucial position can be measured instantaneously with a mechanical position sensor.

V. EXPERIMENTAL RESULTS

Figure 6 demonstrates the experimental test rig which comprises a star-connected 5Φ BLDC Motor, a Half-Bridge IGBT-Based Inverter, and a DC Generator as the load. A 32-bit floating-point DSP (TMS320F28335) joint with an FPGA (XC3S500E) is exploited for the implementation of the overall control scheme. The clock rate of the FPGA is configured to 25MHz, the pulse counter works in an up/down counting mode with the time period register being 0xFFFF. The pulse counter is incremented/decremented by 52 per FPGA clock cycle, and this indicates the PWM frequency can only be about 10.30kHz in this case which is unfortunately not an integer. A synchronization event is generated when the counter hits the preset timer period and it further signals the ADC (or DSP) to start a conversion. In the meantime, the PWM comparator is reloaded, which implies that the typical single PWM-uploading mode is adopted in this work. On completion of the conversion, the CPU core inside the DSP is interrupted to execute the proposed control scheme. An optical encoder is mounted on the shaft to measure the actual rotor position for comparison with the estimate. The rotational inertia of this drive is about $0.12\text{kg}\cdot\text{m}^2$, the DC-link voltage is about 200V, and the HF square-wave current is 20V/257.5Hz (which is 1/4 of the PWM frequency).

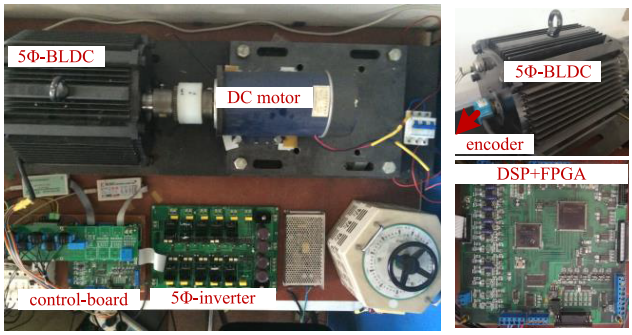

FIGURE 6. Experimental test rig.

The system delay, which is supposed to be 1.5 sampling periods in the previous literature [17], [29], has been compensated for during implementing the conventional sensorless control. Contrast experiments with the proposed method are also carried out. Some other parameters of this 5Φ BLDC are referred to Table 1.

TABLE 1. Motor parameters.

Symbol	Quantity	Value
Ψ_{m1}	fundamental rotor flux	0.535872 Wb
Ψ_{m3}	third harmonic rotor flux	0.033492 Wb
L_d	d-axis inductance	6.54 mH
L_q	q-axis inductance	8.32 mH
L_{13}	Mutual inductance between two subspaces	0.3 mH
L_{d3}	d_3-axis inductance	1.34 mH
L_{q3}	q_3-axis inductance	2.06mH

Figure 7 evolves the experimental procedure for implementing the proposed sensorless control. As aforementioned, $\Delta\theta$-related information, $\varepsilon(\Delta\theta)$, is reflected by the amplitude of the target signal in $I_{\hat{q}h}$, and an LIA is used to identify the target signal from the surrounding noises. In Figure 7(a), a standard reference, H_{ref}, is obtained by phase-locking of the measured d-axis HF current, $I_{\hat{d}h}$, and this reference is further utilized to demodulate $\Delta\theta$ from the measured q-axis HF current. In Figure 7(a),$I_{\hat{q}h}$, which is the combination of the target signal and disturbances, is multiplied by HF_{ref}. Consequently, the target signal becomes DC and all disturbances become twice the injection frequencies. Then with an LPF, all high-frequencies are remarkably attenuated. In Figure 7(b) the filtered DC component is sent to a position observer, and then one can obtain the position and speed estimates. Since the d-axis current is delayed concurrently with the q-axis current given the same hardware and software configurations, this means no time delay between them.

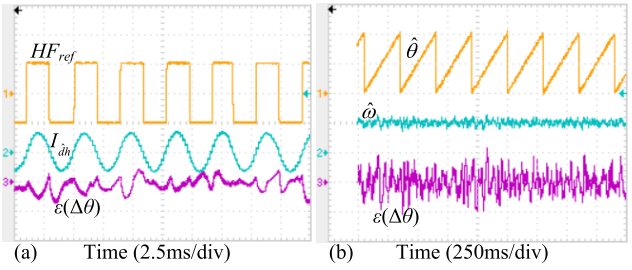

FIGURE 7. The experimental implementation of $\Delta\theta$-demodulation and position acquisition in the proposed method. (a)$\Delta\theta$-demodulation, and (b) position acquisition. HF_{ref} is scaled to 1/div, $I_{\hat{d}h}$ scaled to 2.5A/div, $\varepsilon(\Delta\theta)$ scaled to 0.5deg/div, the position estimate scaled to 180deg/div, the speed estimate scaled to 100rpm.

Figure 8 reveals the motor starting test under, respectively, the conventional and proposed methods. In the figure, the negative zero-crossing point of i_A indicates the origin point of the rotor position, and a trapezoidal phase current is generated to increase the torque density. In this comparison,

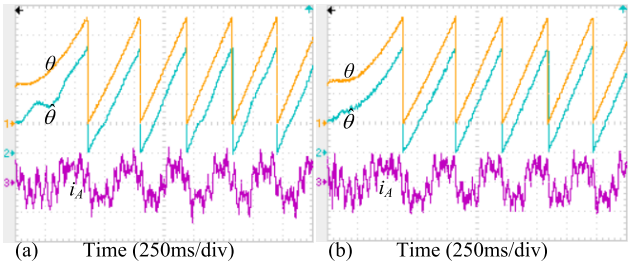

FIGURE 8. Waveforms of motor starting with 30° initial error in position estimate under (a) the conventional method, and (b) the proposed method. The position angular is scaled to 100 deg/div, i_A scaled to 5A/div.

an initial position error of 30°, which corresponds to the resolution of a binary hall-effect position sensor, is used to overwrite the initial value of the position observer. From Figure 8(a), it takes 0.3s for the motor to successfully start under the conventional method. However, from Figure 8(b) the settling time is only 0.12s which is more than halved, and this is owing to that the standard reference for $\Delta\theta$ extraction is always in phase with the target signal (or anti-phased, depending on the estimated d-axis lags behind or leads ahead of the actual d-axis).

Figure 9 refers to the position estimation at 85 rpm under, respectively, the conventional and proposed methods. From Figure 9(a), the position estimation error is up to 40° in the conventional method and some oscillations are present probably due to the unmodelled time delay. From Figure 9(b), the estimation error always stabilizes at 10° and this is attributed to fact that $\Delta\theta$ can be precisely captured with the LIA, and this also confirms the superiority of the proposed method.

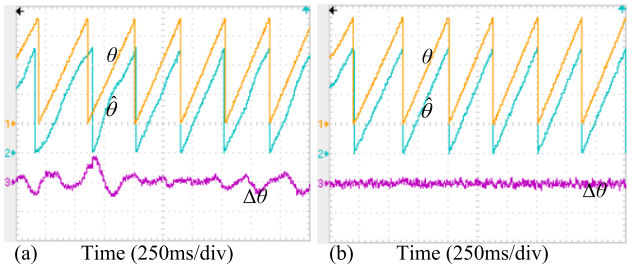

FIGURE 9. Waveforms of the estimated and actual positions in the steady state under (a) the conventional method, and (b) the proposed method. The position angular is scaled to 100 deg/div, $\Delta\theta$ scaled to 50 deg/div.

Figure 10 refers to motor reversing in a constant torque control mode under, respectively, the conventional and proposed methods. In this comparison, a torque reverse command is issued after the motor entering the steady state of sensorless control. From Figures 10(c) and (d), it is evident that the transient process lasts 250ms in the motor reversing. From Figure 10(a), the position estimate deviates up to 35 degrees from the actual position during the transient state. The fluctuation of the position estimation error can be explained by the speed estimate of Figure 10(c) which is incapable to follow up the actual speed in the transient state. However, in Figure 10(b) the motor reversing is much smoother, and

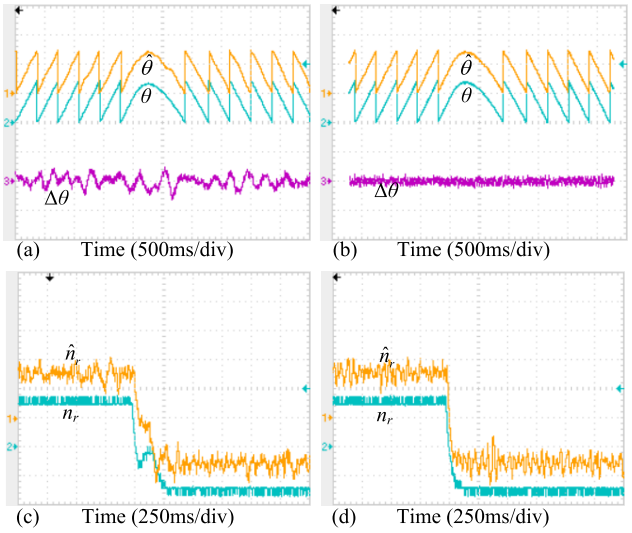

FIGURE 10. Motor reversing test in the constant torque mode. (a) the position behavior under the conventional method; (b) the position behavior under the proposed method; (c) the speed behavior under the conventional method; and (d) the speed behavior under the proposed method. The position angular is scaled to 240 deg/div, $\Delta\theta$ scaled to 50 deg/div, motor speed scaled to 50 rpm/div.

the speed estimate always follows the actual speed swiftly as shown in Figure 10(d). In both cases, the motor reversing can be accomplished, however, position re-tracking performance in the event of the internal disturbance is much desirable under the proposed method.

Figure 11 shows the motor performance in response to the load disturbance under, respectively, the conventional and proposed methods. In this experiment, the speed loop is closed with the speed estimate and then loading is exerted after the motor entering the steady state. Since the speed estimate is with lots of HF ripples, an LPF is firstly used to filter out these undesirable ripples and then the speed estimate after the LPF is fed back to the speed PI regulator. From Figure 11, it takes the motor about 750ms in both cases to re-track the predefined speed command in the presence of the external disturbance, and the speed response is sluggish. The slow dynamic of motor speed is caused by the inclusion of LPF_3 which, however, is unavoidable for robust speed control. The cut-off frequency of LPF is 15Hz which guarantees that most ripples are sufficiently rejected. Nevertheless, the speed

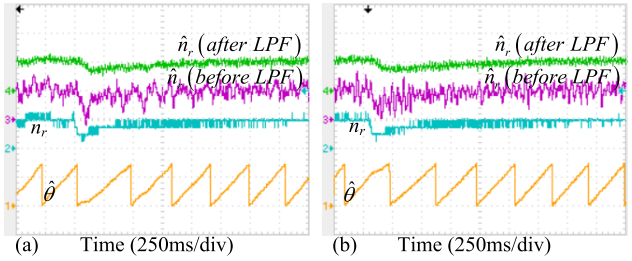

FIGURE 11. Load disturbance test under. (a) under the conventional method; and (b) under the proposed method. The position angular is scaled to 240 deg/div, motor speed scaled to 100 rpm/div.

behavior under the proposed method is more desirable in terms of the speed and/or position fluctuation.

Figure 12 shows motor reversing with the speed PI regulator under, respectively, the conventional and the proposed methods. In this test, the speed estimate, which is also after LPF_3, is fed back to the PI controller. From Figure 12(a), the speed estimate deviates the actual speed too much in the transient state. Whereas in the proposed method the speed estimate is well able to re-track the real motor speed, and the position estimate is, therefore, quite smooth as evident in Figure 12(b). The speed settling time in both cases is up to 500ms which is restricted to LPF_3. Consequently, the superiority of the proposed sensorless control is confirmed.

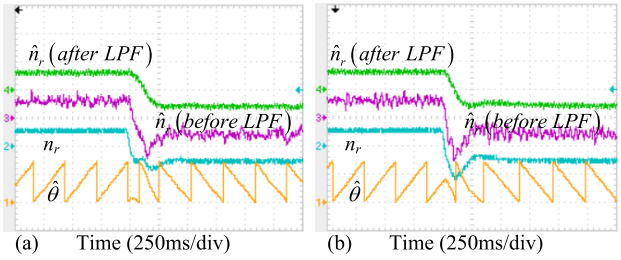

FIGURE 12. Motor reversing test with the speed closed-loop control under (a) position performance the conventional method; and (b) the proposed method. The position angular is scaled to 240 deg/div, motor speed scaled to 100 rpm/div.

Figure 13 refers to the steady state position estimation error when the motor is operated at different rpm from 0 to the scheduled speed. In this figure, the absolute errors are utilized to assess the sensorless control performance under different sensorless controls. From Figure 13, in both cases, the position estimation errors are smaller at low speeds and then increase along with the motor speed, and this coincides with common sense that HF-based sensorless control is most effective in the low-speed region. The estimation error under the proposed method ranges from 8.2 deg to 10.5 deg, whereas this error is between 12 deg to 24 deg under the classical method, and thus it is safe to conclude that the proposed sensorless control is much more superior.

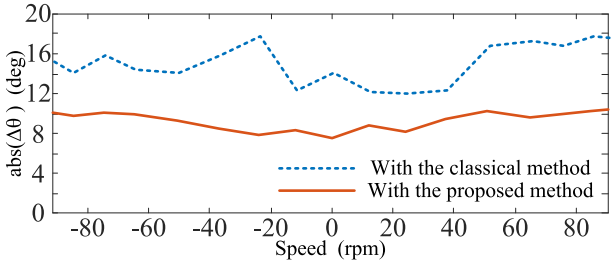

FIGURE 13. The trend of position estimation error under different speeds.

VI. CONCLUSION

This paper presented a more comprehensive high-frequency (HF) model to perform the sensorless control for a general 5Φ BLDC, instead of using a simplified static HF model employed in the previous works. A novel interpretation of the motor HF model from the sinusoidal internal model was conducted incorporating system delay and phase resistance. Accordingly, a standard reference, via phase locking of the measured d-axis current, was utilized for $\Delta\theta$-extraction from the measured q-axis current. Thanks to this, the system delay can be offset by using the measured d-axis HF current, the d-axis low pass filter can be canceled, and the injection frequency was also possible to be lowered. The execution time of the proposed method in a DSP does even not increase when a square-wave voltage injection is adopted which is more resource-saving than the conventional sine/cosine function. Experimental testing of the proposed HF injection was conducted and compared with the conventional method (with a certain digital delay compensation), and the results indicate that the position estimation error under the proposed method can be remarkably improved.

REFERENCES

[1] B. Tian, Q.-T. An, J.-D. Duan, D.-Y. Sun, L. Sun, and D. Semenov, "Decoupled modeling and nonlinear speed control for five-phase PM motor under single-phase open fault," *IEEE Trans. Power Electron.*, vol. 32, no. 7, pp. 5473–5486, Jul. 2017.
[2] L. Zhang, Y. Fan, C. Li, A. Nied, and M. Cheng, "Fault-tolerant sensorless control of a five-phase FTFSCW-IPM motor based on a wide-speed strong-robustness sliding mode observer," *IEEE Trans. Energy Convers.*, vol. 33, no. 1, pp. 87–95, Mar. 2018.
[3] A. Mohammadpour and L. Parsa, "Global fault-tolerant control technique for multiphase permanent-magnet machines," *IEEE Trans. Ind. Appl.*, vol. 51, no. 1, pp. 178–186, Jan./Feb. 2015.
[4] A. Mohammadpour and L. Parsa, "A unified fault-tolerant current control approach for five-phase PM motors with trapezoidal back EMF under different stator winding connections," *IEEE Trans. Power Electron.*, vol. 28, no. 7, pp. 3517–3527, Jul. 2013.
[5] H. Guzman, F. Barrero, and M. J. Duran, "IGBT-gating failure effect on a fault-tolerant predictive current-controlled five-phase induction motor drive," *IEEE Trans. Ind. Electron.*, vol. 62, no. 1, pp. 15–20, Jan. 2015.
[6] B. Tian, Q.-T. An, J.-D. Duan, D. Semenov, D.-Y. Sun, and L. Sun, "Cancellation of torque ripples with FOC strategy under two-phase failures of the five-phase PM motor," *IEEE Trans. Power Electron.*, vol. 32, no. 7, pp. 5459–5472, Jul. 2017.
[7] R. Hyung-Min, J.-W. Kim, and S.-K. Sul, "Synchronous frame current control of multi-phase synchronous motor. Part I. Modeling and current control based on multiple d-q spaces concept under balanced condition," in *Proc. Conf. Rec. IEEE Ind. Appl. Conf., 39th IAS Annu. Meeting*, vol. 1, Oct. 2004, pp. 1–63.
[8] E. B. Sedrine, J. Ojeda, M. Gabsi, and I. Slama-Belkhodja, "Fault-tolerant control using the GA optimization considering the reluctance torque of a five-phase flux switching machine," *IEEE Trans. Energy Convers.*, vol. 30, no. 3, pp. 927–938, Sep. 2015.
[9] G. Zhang, G. Wang, D. Xu, and N. Zhao, "ADALINE-network-based PLL for position sensorless interior permanent magnet synchronous motor drives," *IEEE Trans. Power Electron.*, vol. 31, no. 2, pp. 1450–1460, Feb. 2016.
[10] G. Feng, C. Lai, K. L. V. Iyer, and N. C. Kar, "Improved high-frequency voltage injection based permanent magnet temperature estimation for PMSM condition monitoring for EV applications," *IEEE Trans. Veh. Technol.*, vol. 67, no. 1, pp. 216–225, Jan. 2018.
[11] B. Du, S. Wu, S. Han, and S. Cui, "Application of linear active disturbance rejection controller for sensorless control of internal permanent-magnet synchronous motor," *IEEE Trans. Ind. Electron.*, vol. 63, no. 5, pp. 3019–3027, May 2016.
[12] G. Zhang, G. Wang, H. Zhang, H. Wang, G. Bi, X. Zhang, and D. Xu, "Pseudorandom-frequency sinusoidal injection for position sensorless IPMSM drives considering sample and hold effect," *IEEE Trans. Power Electron.*, vol. 34, no. 10, pp. 9929–9941, Oct. 2019.

[13] T. Nimura, S. Doki, and M. Fujitsuna, "Position sensorless control of PMSM with a low-frequency signal injection," in *Proc. Int. Power Electron. Conf.*, May 2014, pp. 3079–3084.
[14] Y.-D. Yoon, S.-K. Sul, S. Morimoto, and K. Ide, "High-bandwidth sensorless algorithm for AC machines based on square-wave-type voltage injection," *IEEE Trans. Ind. Appl.*, vol. 47, no. 3, pp. 1361–1370, May/Jun. 2011.
[15] G. Zhang, G. Wang, B. Yuan, R. Liu, and D. Xu, "Active disturbance rejection control strategy for signal injection-based sensorless IPMSM drives," *IEEE Trans. Transp. Electrific.*, vol. 4, no. 1, pp. 330–339, Mar. 2018.
[16] X. Wu, "Initial rotor position detection for sensorless interior PMSM with square-wave voltage injection," *IEEE Trans. Magn.*, vol. 53, no. 11, Nov. 2017, Art. no. 8112104.
[17] G. Wang, D. Xiao, G. Zhang, C. Li, X. Zhang, and D. Xu, "Sensorless control scheme of IPMSMs using HF orthogonal square-wave voltage injection into a stationary reference frame," *IEEE Trans. Power Electron.*, vol. 34, no. 3, pp. 2573–2584, Jun. 2019.
[18] H. Zhang, W. Liu, Z. Chen, G. Luo, J. Liu, and D. Zhao, "Asymmetric space vector modulation for PMSM sensorless drives based on square-wave voltage-injection method," *IEEE Trans. Ind. Appl.*, vol. 54, no. 2, pp. 1425–1436, Mar./Apr. 2018.
[19] A. Yousefi-Talouki, P. Pescetto, G. Pellegrino, and I. Boldea, "Combined active flux and high-frequency injection methods for sensorless direct-flux vector control of synchronous reluctance machines," *IEEE Trans. Power Electron.*, vol. 33, no. 3, pp. 2447–2457, Mar. 2018.
[20] J. Lu, Y. Hu, X. Zhang, Z. Wang, J. Liu, and C. Gan, "High-frequency voltage injection sensorless control technique for IPMSMs fed by a three-phase four-switch inverter with a single current sensor," *IEEE/ASME Trans. Mechatronics*, vol. 23, no. 2, pp. 758–768, Apr. 2018.
[21] W. Qian, X. Zhang, F. Jin, H. Bai, D. Lu, and B. Cheng, "Using high-control-bandwidth FPGA and sic inverters to enhance high-frequency injection sensorless control in interior permanent magnet synchronous machine," *IEEE Access*, vol. 6, pp. 42454–42466, 2018.
[22] B. Du, Z. Tianxu, S. Han, L. Song, and S. Cui, "Sensorless control strategy for IPMSM to reduce audible noise by variable frequency current injection," *IEEE Trans. Ind. Electron.*, vol. 67, no. 2, pp. 1149–1159, Feb. 2020.
[23] G. Zhang, G. Wang, H. Wang, D. Xiao, L. Li, and D. Xu, "Pseudorandom-frequency sinusoidal injection based sensorless IPMSM drives with tolerance for system delays," *IEEE Trans. Power Electron.*, vol. 34, no. 4, pp. 3623–3632, Apr. 2019.
[24] G. Wang, J. Kuang, N. Zhao, G. Zhang, and D. Xu, "Rotor position estimation of PMSM in low-speed region and standstill using zero-voltage vector injection," *IEEE Trans. Power Electron.*, vol. 33, no. 9, pp. 7948–7958, Sep. 2018.
[25] G. Wang, D. Xiao, N. Zhao, X. Zhang, W. Wang, and D. Xu, "Low-frequency pulse voltage injection scheme-based sensorless control of IPMSM drives for audible noise reduction," *IEEE Trans. Ind. Electron.*, vol. 64, no. 11, pp. 8415–8426, Nov. 2017.
[26] H. A. Toliyat, M. M. Rahimian, and T. A. Lipo, "dq modeling of five phase synchronous reluctance machines including third harmonic of air-gap MMF," in *Proc. Conf. Rec. IEEE Ind. Appl. Soc. Annu. Meeting*, vol. 1, Sep./Oct. 1991, pp. 231–237.
[27] B. Tian, G. Mirzaeva, Q.-T. An, L. Sun, and D. Semenov, "Fault-tolerant control of a five-phase permanent magnet synchronous motor for industry applications," *IEEE Trans. Ind. Appl.*, vol. 54, no. 4, pp. 3943–3952, Jul./Aug. 2018.
[28] G. Wang, H. Zhou, N. Zhao, C. Li, and D. Xu, "Sensorless control of IPMSM drives using a pseudo-random phase-switching fixed-frequency signal injection scheme," *IEEE Trans. Ind. Electron.*, vol. 65, no. 10, pp. 7660–7671, Oct. 2018.
[29] G. Wang, L. Yang, B. Yuan, B. Wang, G. Zhang, and D. Xu, "Pseudo-random high-frequency square-wave voltage injection based sensorless control of IPMSM drives for audible noise reduction," *IEEE Trans. Ind. Electron.*, vol. 63, no. 12, pp. 7423–7433, Dec. 2016.
[30] G. Zhang, G. Wang, D. Xu, and Y. Yu, "Discrete-time low-frequency-ratio synchronous-frame full-order observer for position sensorless IPMSM drives," *IEEE J. Emerg. Sel. Topics Power Electron.*, vol. 5, no. 2, pp. 870–879, Jun. 2017.
[31] C. Zou, B. Liu, S. Duan, and R. Li, "Influence of delay on system stability and delay optimization of grid-connected inverters with LCL filter," *IEEE Trans. Ind. Informat.*, vol. 10, no. 3, pp. 1775–1784, Aug. 2014.
[32] S. Fukuda and T. Yoda, "A novel current-tracking method for active filters based on a sinusoidal internal model [for PWM invertors]," *IEEE Trans. Ind. Appl.*, vol. 37, no. 3, pp. 888–895, May/Jun. 2001.
[33] J. Park, Y.-J. Moon, M.-G. Jeong, J.-G. Kang, S.-H. Kim, J.-C. Gong, and C. Yoo, "Quasi-resonant (QR) controller with adaptive switching frequency reduction scheme for flyback converter," *IEEE Trans. Ind. Electron.*, vol. 63, no. 6, pp. 3571–3581, Jun. 2016.
[34] F. Paz and M. Ordonez, "High-performance solar MPPT using switching ripple identification based on a lock-in amplifier," *IEEE Trans. Ind. Electron.*, vol. 63, no. 6, pp. 3595–3604, Jun. 2016.
[35] M. O. Sonnaillon, R. Urteaga, and F. J. Bonetto, "High-frequency digital lock-in amplifier using random sampling," *IEEE Trans. Instrum. Meas.*, vol. 57, no. 3, pp. 616–621, Mar. 2008.

BING TIAN received the B.S. and M.S. degrees in electrical engineering from Harbin Engineering University, Harbin, China, in 2011 and 2013, respectively, and the Ph.D. degree in electrical engineering from the Harbin Institute of Technology, Harbin, China, in 2018. He is currently a Postdoctoral Researcher with the Department of Engineering Cybernetics, Norwegian University of Science and Technology (NTNU). His research interests include PM electric machines and drives, and renewable energy.

QUN-TAO AN (S'10–M'11) received the B.S. degree in electrical engineering from the Harbin University of Science and Technology, Harbin, China, in 2004, and the M.S. and Ph.D. degrees in electrical engineering from the Harbin Institute of Technology, Harbin, in 2006 and 2011, respectively. From 2009 to 2010, he was an Honorary Fellow with the Wisconsin Electric Machines and Power Electronics Consortium, University of Wisconsin-Madison. Since 2009, he has been with the Faculty of the Harbin Institute of Technology, and he is currently an Associate Professor. His research interests include electric machines and drives, power electronics, and energy storage technology.

MARTA MOLINAS (M'94) received the Diploma degree in electromechanical engineering from the National University of Asuncion, Asuncion, Paraguay, in 1992, the M.Eng. degree from Ryukyu University, Japan, in 1997, and the D.Eng. degree from the Tokyo Institute of Technology, Tokyo, Japan, in 2000. She was a Guest Researcher with the University of Padova, Padova, Italy, in 1998. From 2004 to 2007, she was a Postdoctoral Researcher with the Norwegian University of Science and Technology (NTNU), where she was a Professor with the Department of Electric Power Engineering, from 2008 to 2014. She is currently a Professor with the Department of Engineering Cybernetics, NTNU. Her research interests include stability of power electronics systems, harmonics, instantaneous frequency, and non-stationary signals from the human and the machine. She was an AdCom member of the IEEE Power Electronics Society, from 2009 to 2011. She is an Associate Editor for the IEEE Journal JESTPE and IEEE PELS Transactions, and an Editor of the IEEE TRANSACTIONS ON ENERGY CONVERSION.